

Supporting Information: Nanoparticle separation based on size-dependent aggregation of nanoparticles due to the critical Casimir effect

Hongyu Guo,^{†,‡} Gheorghe Stan,[§] and Yun Liu^{*,†,‡,||}

[†]Center for Neutron Research, National Institute of Standards and Technology, Gaithersburg, Maryland 20899, United States; [‡]Department of Chemical and Biomolecular Engineering, University of Delaware, Newark, Delaware 19716, United States; [§]Materials Measurement Science Division, National Institute of Standards and Technology, Gaithersburg, Maryland 20899, United States; ^{||}Department of Physics and Astronomy, University of Delaware, Newark, Delaware 19716, United States

*e-mail: yunliu@udel.edu or yunliu@nist.gov

I. Materials and Sample Preparation¹

I.1 Materials

Silica nanoparticles (NPs) with different sizes were purchased from Sigma-Aldrich: Ludox SM-30 (P1 NPs with the radius of 5 nm) and Ludox TM-50 (P2 NPs with the radius of 13 nm). Both were used as received. Mass fractions of silica NP stock solutions were 30% for Ludox SM-30 and 50% for Ludox TM-50, and were confirmed by our own measurements. Samples were prepared by dispersing silica NPs in 2,6-

lutidine/water mixtures with different lutidine concentrations. Both Ludox SM-30 and Ludox TM-50 NPs were claimed to be monodispersed by the manufacturer. 2,6-dimethylpyridine (lutidine) (> 99%) was purchased from Sigma-Aldrich too and used as received. Milli-Q water (18.2 M Ω -cm) was used for samples prepared with H₂O. D₂O (> 99.9%) was purchased from Cambridge Isotope (Cambridge Isotope Laboratories, Inc., Tewksbury, MA). The densities of H₂O, D₂O, and lutidine used in our calculations are 1.000, 1.106, and 0.925 g/cm³, respectively. The estimated volume fraction of silica NPs during the sample preparation was based on silica density to be 2.648 g/cm³ (quartz density). However,

¹Identification of a commercial product in this paper does not imply recommendation or endorsement by the National Institute of Standards and Technology (NIST), nor does it imply that the product is necessarily the best for the stated purpose.

it is known that the density of silica NPs is smaller. But this does not affect the conclusions of our paper and data analysis.

I.2 Sample preparations for atomic force microscopy (AFM), dynamic light scattering (DLS), and small angle neutron scattering (SANS) experiments

All samples before the purification were prepared to have the mole fraction of lutidine in the lutidine/water mixture, w , at 0.0899 (corresponding to a lutidine mass fraction at 0.37 for the lutidine/H₂O solvent). (This lutidine concentration is chosen due to the large temperature window between T_a and T_s . Other lutidine concentrations can be also chosen to purify NPs.) Because mixing lutidine with water is an exothermic process, we first mixed water and Ludox to prepare low particle concentration solutions before adding lutidine to the solutions with sufficient stirring.

For *in-situ* SANS experiments (Fig. 2 and Fig. 3 in the main text and Fig. S4 in this SI) water was a mixture of D₂O and H₂O with a mole ratio $M_{D_2O}/M_{H_2O} = 0.328$. At this ratio of D₂O and H₂O, the coherent neutron scattering length density (SLD) of water matches the SLD of lutidine so that during our *in-situ* SANS experiments, there are no contributions from the solvent density fluctuations to the coherent SANS signals. The change of the ratio between D₂O and H₂O

slightly shifts the critical point of lutidine/water mixture. For $M_{D_2O}/M_{H_2O} = 0.328$, T_c is shifted to 32.4 °C. But this does not affect our experimental conclusions.

For the *ex-situ* experiments showed in Fig. 4 and Fig. 5 in the main text, the solvents of all samples after purification were further exchanged with pure D₂O so the information of solution viscosity and the refractive index is readily available. These parameters are needed in DLS experiments to estimate r_h shown in Fig. 4.¹ D₂O was used to minimize the incoherent background of *ex-situ* SANS data which were used to obtain r_g shown in Fig. 4. To be consistent, the same sample preparation procedure was also used for the AFM measurements. For the DLS and SANS experiments shown in Fig. 4, the volume fractions of final processed samples were diluted to be less than 0.1%.

I.3 Adsorption preference of solvent molecules on Ludox particle surfaces

As reported previously² and confirmed by our experiments,³ Ludox particles we used have a strong preference for water instead of lutidine, which determined the range of lutidine concentration we chose for this study. Detailed information of the preferential adsorption of water on silica particle surfaces have been studied previously.³

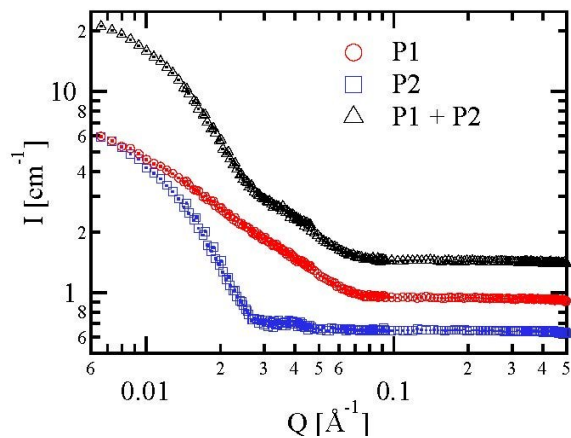


Figure S1 Same figure as the Fig. 2 in the main text, which is replotted here by scaling some patterns vertically so that the data at high Q can be seen more clearly. SANS data of three different NP samples measured at room temperature. 0.4% volume fraction of P1 NPs (red circles), 0.1% volume fraction of P2 NPs (blue squares), and the mixture of P1 (0.4% volume fraction) and P2 (0.1% volume fraction) NPs (black triangles) are dispersed in the matched lutidine/water solvents with $w = 0.0899$ (corresponding to 37% mass fraction for the lutidine/H₂O mixture). The error bars represent one standard deviation (SD) and are smaller than the symbols. Each curve contains 220 data points.

II. Small angle neutron scattering (SANS) Experiments

SANS measurements were conducted on NGB30mSANS, NG7SANS, and nSoft 10m SANS at the NIST Center for Neutron Research (NCNR). SANS data were reduced and analyzed using a software package provided by NCNR.⁴

As explained in the main text, SANS patterns are very sensitive to the change of particle size and size distributions in solutions. We replot the Fig. 2 in main text here (Fig. S1) by offsetting the curves so that the details of high Q can be seen better.

II.1 Contrast variation for the *in-situ* SANS experiments

By taking advantage of different scattering length density (SLD) of H₂O and D₂O, the SLD of water in the lutidine/water binary solvent can be adjusted to that of lutidine. Here, we demonstrate that by correctly mixing the right amount of H₂O and D₂O, the coherent SANS signals of our samples are only from the silica NPs. This method is typically called the contrast variation method in SANS studies.⁵

The SLDs of lutidine, H₂O, and D₂O, are $1.156 \times 10^{-4} \text{ nm}^{-2}$, $-0.561 \times 10^{-4} \text{ nm}^{-2}$, and $6.367 \times 10^{-4} \text{ nm}^{-2}$, respectively. To match the SLD of lutidine using the mixture of H₂O and D₂O, the mole ratio between D₂O and H₂O, $M_{\text{D}_2\text{O}}/M_{\text{H}_2\text{O}}$, should be 0.328. Using D₂O/H₂O mixture instead of pure H₂O will shift the critical point slightly. For $M_{\text{D}_2\text{O}}/M_{\text{H}_2\text{O}} = 0.328$, T_c is shifted to 32.4 °C.

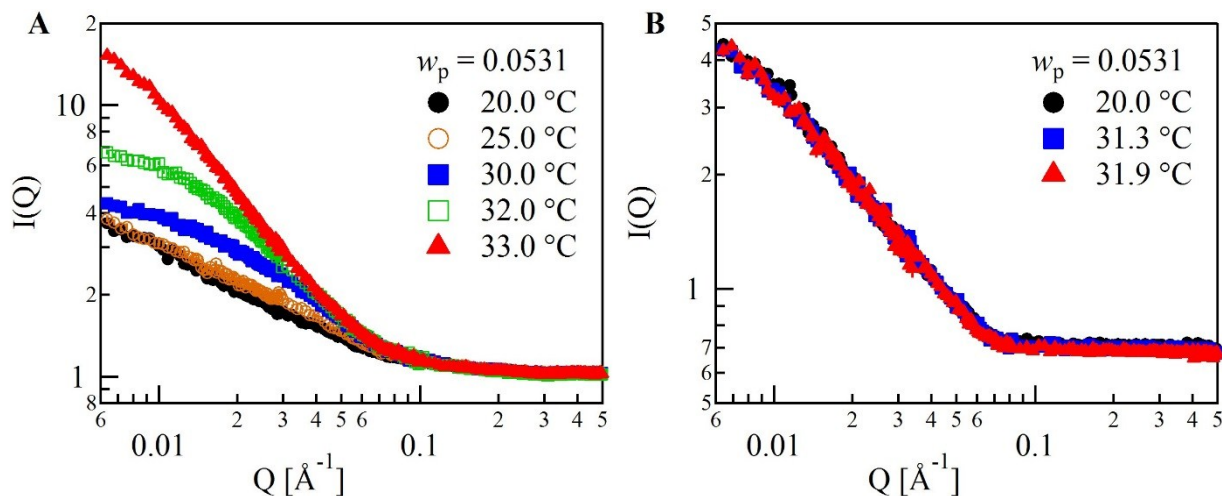


Figure S2. SANS curves of P1 NPs suspended in two lutidine/water mixture with same volume fraction 0.4% and lutidine concentration ($w = 0.0531$) at different temperatures. (This corresponds to 0.25 mass fraction of lutidine in a lutidine/ H_2O solvent.) (A) in mixture of lutidine and pure H_2O . When increasing the temperature, the SANS intensities at low Q became bigger and bigger due to the growing contributions from the solvent density fluctuations. (B) in mixture of lutidine and SLD matched water ($M_{D20}/M_{H2O} = 0.328$). The contributions to the SANS intensities from the solvent density fluctuations were suppressed in contrast matched cases. Also, no NP aggregations were observed since $w < w_c$. This explains that the SANS intensities had no change. Error bars represent one standard deviation and are smaller than the symbols.

To demonstrate the effectiveness of this contrast variation method, SANS results of P1 NPs suspended in two different solvents are shown in Fig. S2. For both samples in Fig. S2, the volume fraction of NPs is maintained at $\phi = 0.4\%$, and lutidine mole fraction, w , is kept at 0.0531 (This corresponds to a lutidine mass fraction at 0.25 in a lutidine/ H_2O solvent). For Fig. S2A, pure H_2O was used to prepare the water/lutidine solvent. The SANS patterns in Fig. S2A thus included the scattering from both silica NPs and the density fluctuations between water and lutidine. When increasing the temperature, the scattering signal from the solvent fluctuation became stronger and stronger resulting in the large increase of the scattering intensity. For Fig. S2B, water was prepared by mixing

the D_2O and H_2O with $M_{D20}/M_{H2O} = 0.328$ so that the SLD of water is the same as that of lutidine. Hence, there was no scattering contrast between water and lutidine. Now SANS signals were not sensitive at all to the solvent fluctuation and were only dependent on the NPs in the solutions. As demonstrated in Fig. S2B, changing temperatures did not change the SANS signals at all. These results also further indicate that for $w < w_c$, silica NPs remain stable in the solvent and do not aggregate in these samples.

II.2 *In-situ* SANS experiments and data analysis

For *in-situ* SANS study shown in Fig. 3 of the main text and Fig. S4, $I(Q)$ were measured at different temperatures. Because the SLD of lutidine was matched by the mixture of D_2O and H_2O , the solvent

fluctuations between lutidine and water were invisible to neutron scattering when the temperature approached $T_s(w)$. Furthermore, since both Sample 1 and Sample 2 were dilute (Sample 1 with 0.4% volume fraction of silica NPs P1, and Sample 2 with 0.4% and 0.1% volume fractions of silica NPs P1 and P2 respectively), we only need to consider the form factor of NPs and assume the inter-particle structure factor to be unity.

The SANS signals can be expressed as

$$I(Q) = \sum_j I_{P_j}(Q) + B_{\text{incoh}}, \quad (1)$$

where Q is the scattering vector and B_{incoh} is the Q -independent background due to mostly the incoherent scattering of our samples. $I_{P_j}(Q)$ represents the coherent signal from j^{th} population of particles and can be expressed as

$$I_{P_j}(Q) = n_j \cdot P_{P_j}(Q), \quad (2)$$

where $n_j = \varphi_j/V_{P_j}$ is the particle number density given by the volume fraction φ_j and the individual particle volume V_{P_j} of j^{th} component of particles. The form factor $P_{P_j}(Q)$ is determined by the shape, size, size distribution, and scattering length density of NPs. $P(Q)$ is related to the Fourier transform of the spatial variation of the local scattering length density $\rho(r)$ inside the scatterer (the particle) compared to the average solvent scattering length density ρ_s ,

$$P(Q) = \left| \int dr e^{iQ \cdot r} [\rho(r) - \rho_s] \right|^2. \quad (3)$$

For monodisperse hard spheres, the form factor is known as⁶

$$P(Q) = \left[\frac{3V(\Delta\rho)(\sin(QR) - QR\cos(QR))}{(QR)^3} \right]^2, \quad (4)$$

where $\Delta\rho = \rho_p - \rho_s$ is the contrast, R is the spherical radius, and V is the spherical volume. When these spherical particles are polydisperse, $P_j(Q) = \varphi_j \langle P_j(Q) \rangle / \langle V_j \rangle$, where the angle bracket denotes an average over the size distribution. For many NPs, the Schulz distribution is commonly used to describe the particle size distribution. The Schulz distribution has two parameters: mean radius R and width σ_R .⁷ In our experiments, it is sufficient to consider our silica NPs as hard spheres with uniform SLD ρ_p and Schulz size distributions. Hence, for this model, the fitting parameters are volume fraction φ , mean radius R , and polydispersity index $f \equiv \sigma_R/R$, when the SLDs of each component are already known. Consistent with our AFM results shown later in Fig. S8, two Schulz distributions were used to model the size distribution of Sample 1. And for Sample 2, we had to use three Schulz distributions to describe the size distribution. The SLD of the solvent is $\rho_s = 1.156 \times 10^{-4} \text{ nm}^{-2}$.

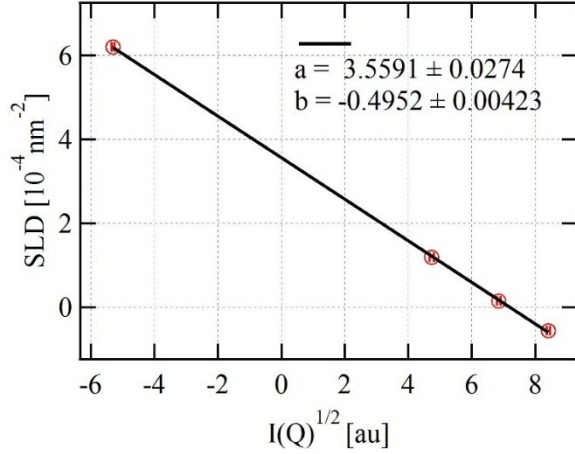


Figure S3. SLD measured with 4 different H₂O/D₂O mixtures as solvents for Sample 1, P1 NPs. Solid line is the linear fitting and the intercept is the measured SLD. Error bars represent one standard deviation.

The SLD of silica NPs, ρ_p , was determined experimentally. A very dilute silica NP sample was prepared in pure water with different mixture ratios of D₂O and H₂O. When the NP volume fraction is kept the same, the square root of the coherent scattering signal, $I(Q)^{1/2}$, measured by SANS is proportional to $\Delta\rho = \rho_p - \rho_s$. Thus, varying ρ_s by changing the mixture ratio of D₂O and H₂O, the SLD for our silica NPs, ρ_p , can be experimentally determined. Fig. S3 shows the results from P1 NPs using four different H₂O/D₂O mixtures as solvents. The intercept of linear fitting is the SLD of the NPs, $\rho_{p1} = 3.56 \times 10^{-4} \text{ nm}^{-2}$. Similarly, we can get SLD of P2 NPs, $\rho_{p2} = 3.45 \times 10^{-4} \text{ nm}^{-2}$. (The mass densities of P1 NPs and P2 NPs can be estimated to be 2.26 g/cm³ and 2.19 g/cm³ for P1 and P2 NPs using the experimentally determined SLDs. These results are consistent with the literature.⁸⁾)

In the main text, the *in-situ* SANS results of Sample 1 are shown in Fig. 3. Here, we show the SANS scattering curves and fitting results of Sample 2 for several temperatures in Fig. S4.

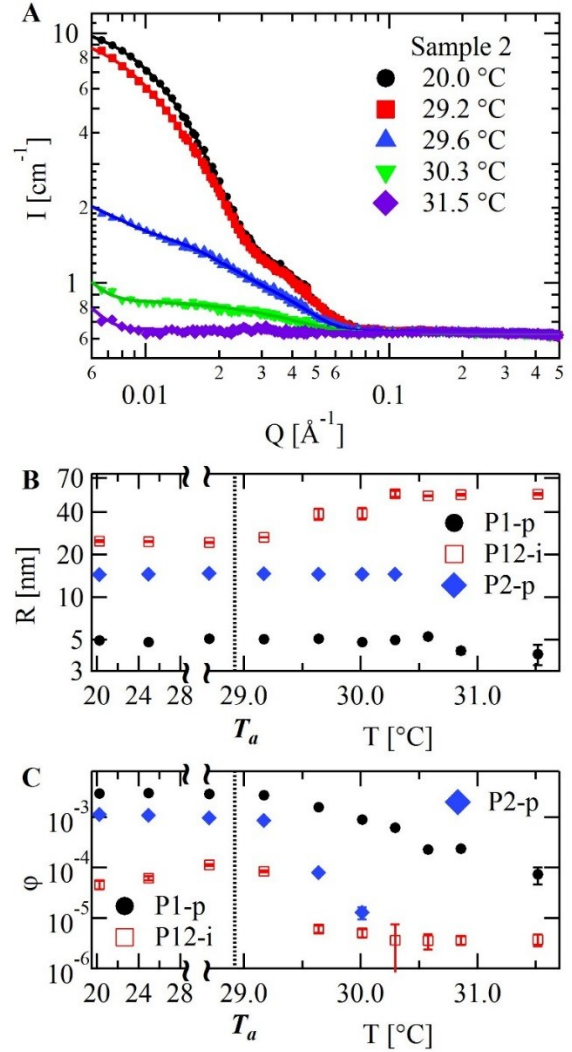


Figure S4. *In-situ* SANS studies of Sample 2. (A) SANS curves in absolute scale at different temperatures. Solid lines are fits to the hard sphere model with Schulz distributions. (B) estimated particle sizes as a function of temperature by fitting SANS curves. The vertical dotted line indicates T_a , above which temperature the precipitates can be observed in samples. (C) estimated particle volume fractions as a function of temperature. The error bars represent one standard deviation.

Consistent with our AFM results shown later in Fig. S8, the best fits of the curves were found when three constituents were considered for the NP system: P1-p for small size NPs (size around 5 nm), P2-p for large size NPs (size around 13 nm), and P12-i for any impurities and aggregations (size larger than 20 nm) from both P1 and P2 populations. The results show strong temperature variation when $T > T_a(w)$, similar to that of Sample 1 reported in Fig. 3 in the main text. The calculated particle sizes and volume fractions of these constituents are shown in Fig. S4B and S4C respectively, where the increase of the sizes of P12-i and the decrease in the volume fractions of P12-i and P2-p indicate strong aggregation for the NPs. The decrease of volume fractions of P12-i and P2-p are due to the precipitation. Such particle size-selective mechanism ensures separation of large particles from small particles. This is consistent with the removal for large size NPs indicated by the AFM measurements (Fig. 5B, and Fig. S8D). The yield of purified P1-p is surprisingly good, at $T = 29.6$ °C, there are more than 53% of P1-p NPs (by comparing the volume fractions) still in solution with the purity to be above 95%. At $T = 30.3$ °C, there are still more than 21% of P1-p

particles remain in solution and the purity is at least 98.5%.

It is noted that the parameters of the Schultz distributions from the SANS fitting is in general more reliable at relatively low temperatures. When the temperature is very high (two highest temperatures for the in-situ experiment studied here), the volume fraction of the P1-i is so small that the parameters for P1-i may not be so reliable and have large relative error bars.

II.3 *Ex-situ* SANS experiments to obtain r_g

For the *ex-situ* SANS experiments showed in Fig. 4 in the main text, the measured scattering intensities were dominated by the form factors of the particles as the volume fractions of NPs in these samples were less than 0.1%. At low- Q limit, the Guinier analysis⁶ can

be applied as $I(Q) \propto \exp\left[-\frac{1}{3}(r_g Q)^2\right]$, where r_g is the radius of gyration of particles. Fig. S5A and S5B show $I(Q)$ of both Sample 1 and Sample 2 measured at room temperature after the purification at different processing temperatures T_p . Fig. S5C and S5D are exemplary Guinier plots for Sample 1 and Sample 2 after purified at $T_p = 29.4$ °C respectively.

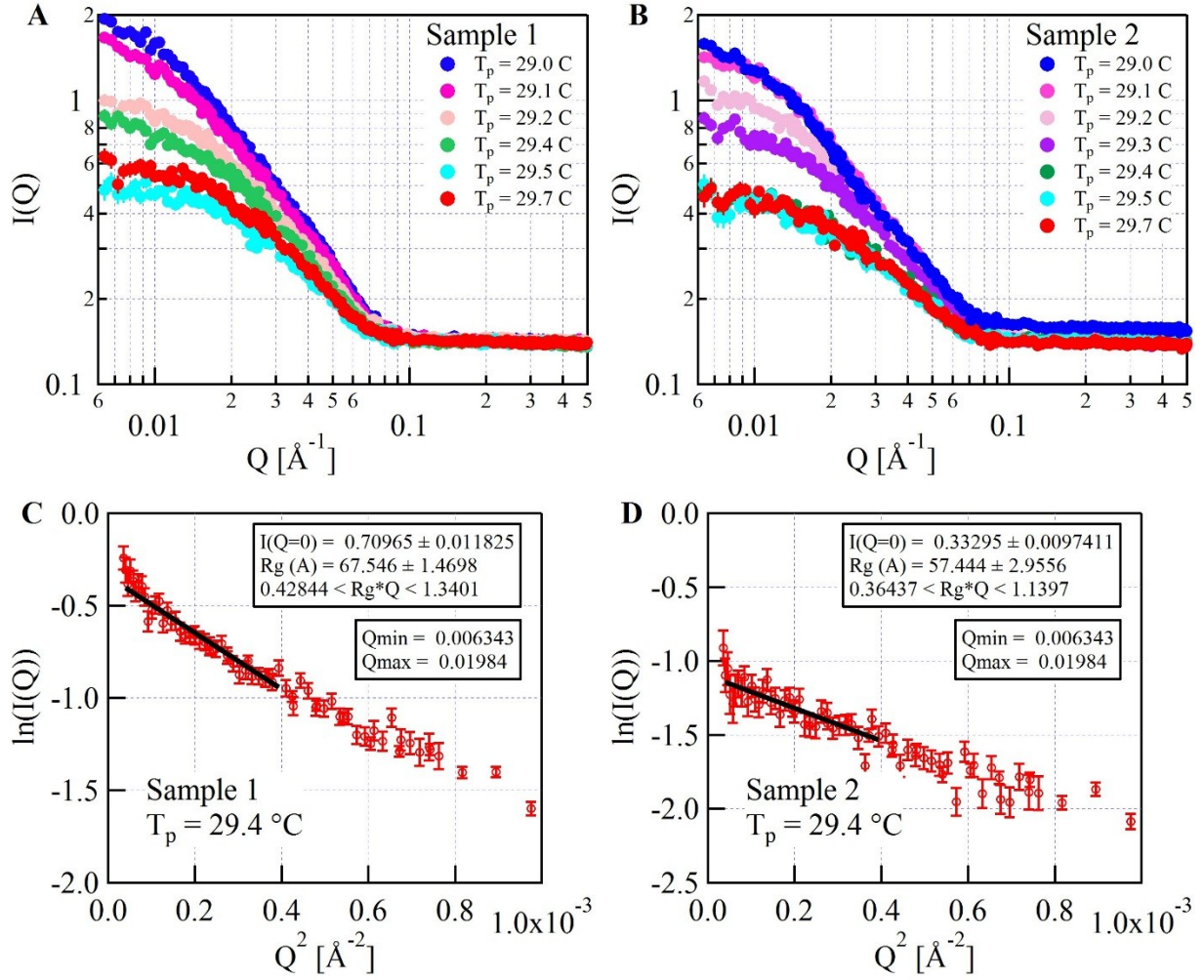


Figure S5. SANS measurements of Sample 1 and 2 at room temperature after processed by our purification method at different T_p . (A) SANS curves of Sample 1. (B) SANS curves of Sample 2. (C) example of Guinier plot for Sample 1 measured at room temperature after processed at $T_p = 29.4$ °C. The black solid line is the linear fitting and gives $r_g = 6.75 \pm 0.15$ nm for this case. (D) example of Guinier plot for Sample 2 measured at room temperature after processed at $T_p = 29.4$ °C. The black solid line is the linear fitting and gives $r_g = 5.74 \pm 0.30$ nm for this case. Error bars represent one SD. For SANS curves in (A) and (B), the error bars are smaller than the symbols.

III. Dynamic light scattering (DLS) measurements

DLS was performed with a DynaPro NanoStar M3300 instrument (Wyatt Technology Corp., Santa Barbara, CA). A standard setup with the fixed scattering angle at $2\theta = 90^\circ$ was used for all measurements. The wavelength of the laser was $\lambda = 663$ nm. In the measurements, the wave vector was defined as $Q =$

$2k_i \sin\theta$, where $k_i = 2n\pi/\lambda$ is the wave vector of the incident light and n is the refractive index of the solution. The decay rate, Γ , was extracted by fitting the measured intensity autocorrelation function with a simple exponential function. Then the diffusion coefficient was calculated by using $D = \Gamma/Q^2$. Based on the Stokes–Einstein equation, the average

hydrodynamic radius was determined by $r_h = k_B T / (6\pi\eta D)$, where k_B is Boltzmann's constant, T is absolute temperature, and η is the dynamic viscosity of the solution. Both the viscosity η and refractive index n are solvent dependent. In our analysis, we used parameters from pure D₂O since the particle volume fractions of final samples were very low for the DLS experiments after the solvent exchange and dilution process.

IV. Atomic force microscopy (AFM) measurements

AFM was performed with a MultiMode 8 Bruker AFM (Bruker, Santa Barbara, CA) operated in amplitude modulation (tapping) scanning mode. Prior to measurements, the calibration of the AFM z-piezo scanner was checked against a few commonly used references across the range from 1 nm to 100 nm. We used three calibration references: 1) Crystallographic 6H-SiC (0001) steps (Ted Pella, Inc., Redding, CA) of nominal step height 0.75 nm (single SiC half-monolayer); 2) TGZ 01 certified calibration grating

(MikroMasch, Tallinn, Estonia) with a mean step height of 19.5 ± 0.8 nm (based on the step height reference standard: NIST 821/261141-99); 3) TGZ 02 certified calibration grating (MikroMasch, Tallinn, Estonia) with a mean step height of 102.9 ± 1.6 nm (based on the step height reference standard: NIST 821/261141-99). The histograms of the AFM height measurements performed on these references are shown in Fig. S6. From these histograms, the mean values and uncertainties of the measured height differences were determined from the central value and half-width at the half-maximum of each Gaussian distribution, respectively. The results of the AFM calibration were collected and plotted in Fig. S6 against the nominal values. As can be seen, by considering the measured and nominal mean values, the largest uncertainty for our z-piezo scanner was 1% at 100 nm.

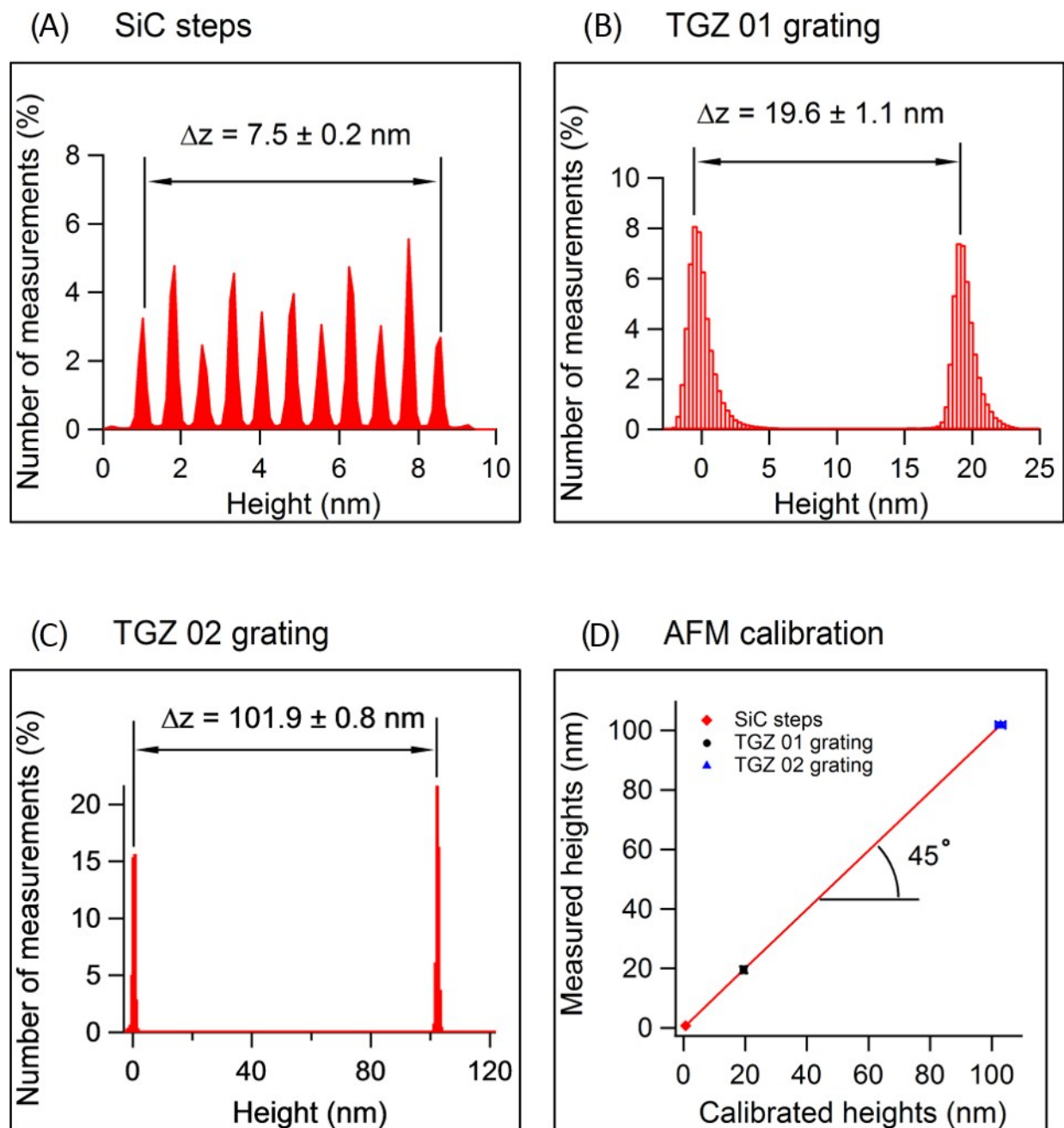


Figure S6. AFM height calibration on various references. (A) across 10 consecutive crystallographic SiC steps (nominal step height 0.75 nm) within a $2\ \mu\text{m} \times 2\ \mu\text{m}$ scanned area. (B) the mean step height of the TGZ 01 grating across five consecutive pitches within a $15\ \mu\text{m} \times 15\ \mu\text{m}$ scanned area. (C) the mean step height of the TGZ 02 grating across five consecutive pitches within a $15\ \mu\text{m} \times 15\ \mu\text{m}$ scanned area. (D) comparison between measured and calibrated heights.

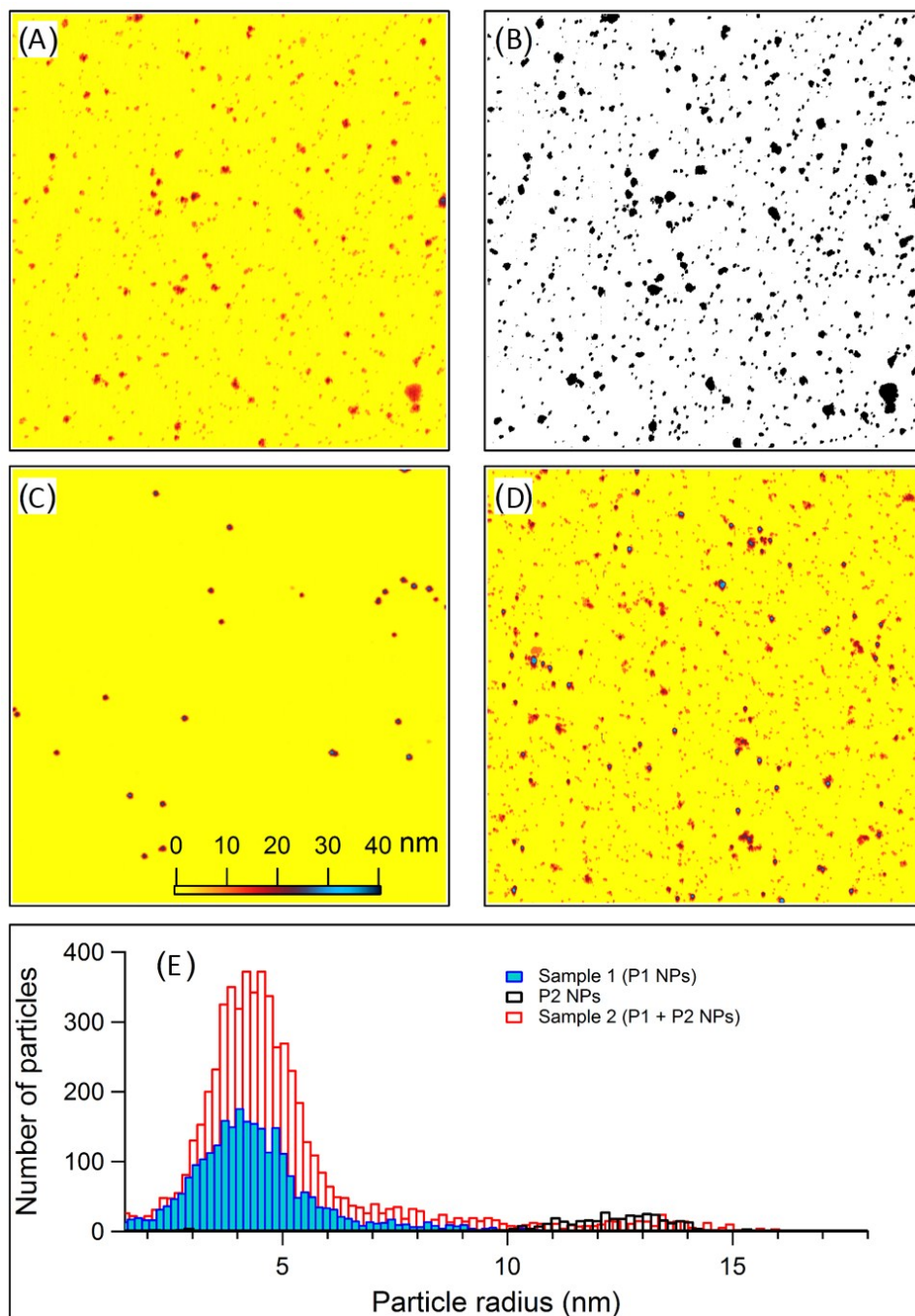


Figure S7. $5\ \mu\text{m} \times 5\ \mu\text{m}$ AFM topographical images of NPs on mica. (A) AFM topographical image of Sample 1 (P1 NPs). (B) the threshold image of the image (A) as it was used to identify and locate all the objects with height above 1 nm from the flat surface of the mica substrate; the heights of the identified objects were then measured to find the NP sizes. (C) AFM topographical image of P2 NPs without any treatment. (D) AFM topographical image of Sample 2 (P1 + P2 NPs). (E) the histograms in terms of the number of particles collected from five AFM topographical images of NPs from Sample 1 (P1 NPs), P2 NPs, and Sample 2 (P1 + P2 NPs), respectively.

The histograms shown in Fig. S7E were the number distributions of particles as a function of the particle

size before the purifications. Note that the distributions are not normalized. For sample 1 (solid

blue histogram), the number distribution is dominated by the main peak at 4.2 nm with a long tail at large values due to the presence of large particles in Sample 1. The distribution of P2 NPs is shown as black histograms in Fig. S7E with the particle size ranging from about 10 nm to about 15 nm. Sample 2 has both P1 and P2 particles. Hence its histograms (red histograms) have the size range from about 2 nm to about 15 nm. Even though the volume fractions of P1 and P2 particles are comparable in Sample 2 (4:1), P1 particles dominate the number distribution of Sample 2 due to the smaller particle sizes.

For many NP applications, such as nanocomposites, the controlling factor for its macroscopic properties is the volume fraction of particles rather than the number density of particles. In addition, scattering measurements are typically weighted by particle volumes. Therefore, the particle volume distributions of Sample 1 and Sample 2 before purifications as a function of the particle size were estimated and are plotted in Fig. S8A and Fig. S8C respectively. The total particle volume for both Sample 1 and Sample 2 is normalized to one. As a comparison, the normalized number distributions are also shown in Fig. S8. The left axis indicates the value for the normalized number distribution while the right axis shows the value for the normalized volume distribution. Because larger particles have larger

volumes, the volume distributions for both Sample 1 and Sample 2 show significantly larger contributions from large particles. Since larger P2 particles are added into Sample 2, a peak emerges in the volume distribution of Sample 2 at 13.6 nm due to the presence of P2 particles. Note that because the number of particles for large particles is relatively small, the estimation of the volume distributions has larger error bars for larger particles.

Based on the volume distribution, there are at least two size populations of NPs in Sample 1 and three populations in Sample 2. Because the estimated particle size is weighted by the particle volume for SANS data, it is thus reasonable to model the particle distribution of Sample 1 with two size populations and Sample 2 with three size populations during the SANS data analysis. After the purification, the volume distributions of NPs in Sample 1 (Fig. S8B) and Sample 2 (Fig. S8D) show that large particles from both Sample 1 and Sample 2 are mostly removed from the solutions. This indicates that our purification method is very efficient.

Note that the particle size distribution obtained by the AFM is a direct measurement result. We have counted many particles in order to have enough statistics for the particle size distribution. However, it is still possible that the particles with very large size

may still have very small number of particles that can be found on the mica surfaces. We thus use the size distribution from the AFM as a guide to model the particle size distribution during the SANS fitting.

However, it should be noted that the size distribution obtained by SANS fitting is biased by the model we choose.

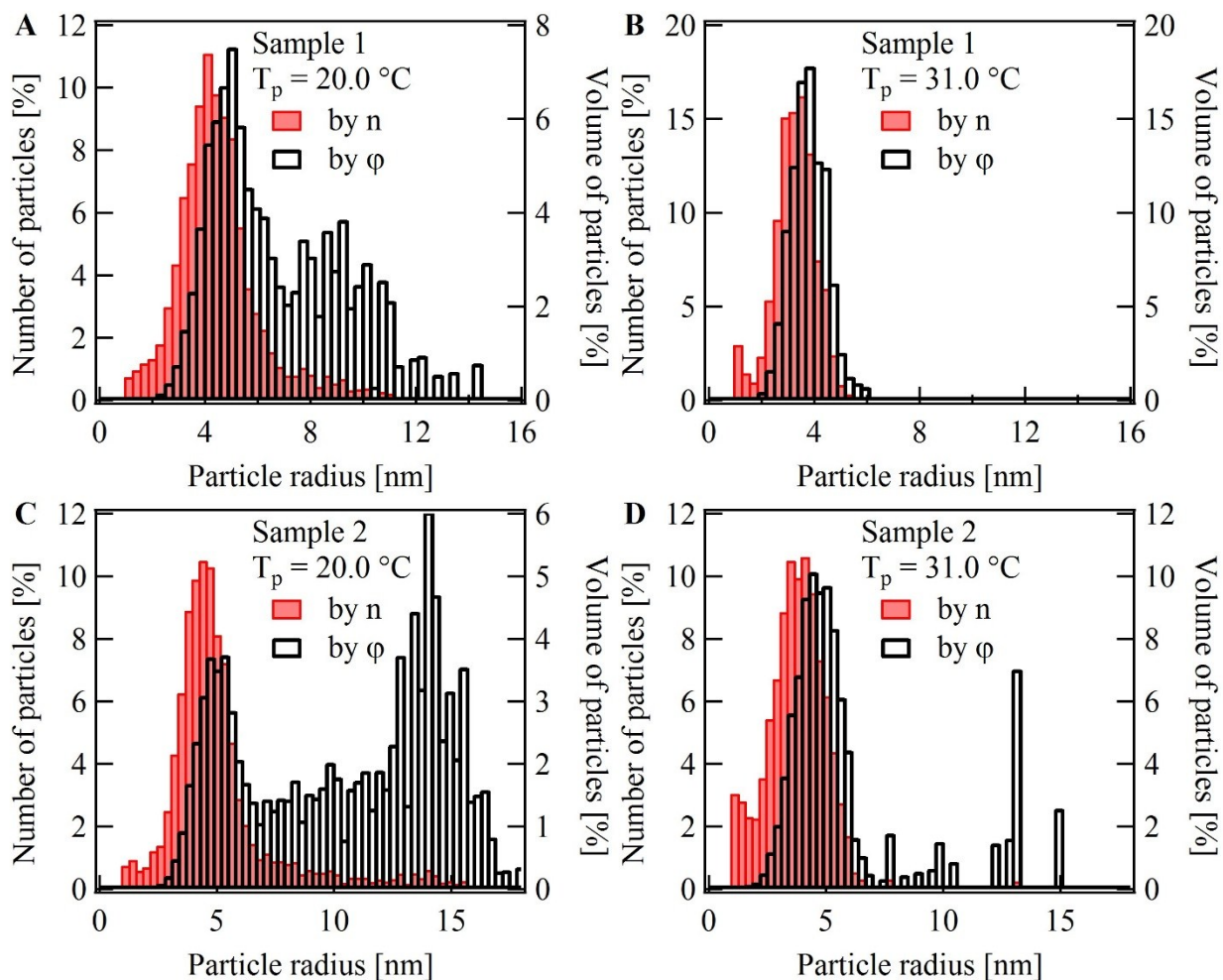


Figure S8. Histograms in terms of the number of particles (red) and the volume of particles (black) collected from five AFM topographical images of NPs from both Sample 1 and Sample 2 at two processing temperatures. The bin size is 0.3 nm and the total numbers of measured particles are larger than 2000 for each histogram. (A) Sample 1 (P1 NPs) at $T_p = 20.0$ °C. (B) Purified Sample 1 with $T_p = 31.0$ °C. (C) Sample 2 (P1 + P2 NPs) at $T_p = 20.0$ °C. (D) Purified Sample 2 with $T_p = 31.0$ °C.

References

- 1 B. Rathke, H. Gröll and D. Woermann, *J. Colloid Interface Sci.*, 1997, **192**, 334–337.
- 2 Y. Jayalakshmi and E. W. Kaler, *Phys. Rev. Lett.*, 1997, **78**, 1379–1382.
- 3 C. E. Bertrand, P. D. Godfrin and Y. Liu, *J. Chem. Phys.*, 2015, **143**, 84704.
- 4 S. R. Kline, *J. Appl. Crystallogr.*, 2006, **39**, 895–900.
- 5 A.-C. Genix and J. Oberdisse, *Curr. Opin. Colloid Interface Sci.*, 2015, **20**, 293–303.
- 6 L. A. Feigin and D. I. Svergun, *Structure Analysis by Small-Angle X-Ray and Neutron Scattering*, Springer US, Boston, MA, 1987.
- 7 M. Kotlarchyk and S.-H. Chen, *J. Chem. Phys.*, 1983, **79**, 2461.

- 8 J. D. F. Ramsay, R. G. Avery and L. Benest,
Faraday Discuss. Chem. Soc., 1983, **76**, 53–63.